

Dissipation engineering of high-stress silicon nitride nanobeams

A. H. Ghadimi, D. J. Wilson, and T. J. Kippenberg

École Polytechnique Fédérale de Lausanne (EPFL), CH-1015 Lausanne, Switzerland

(Dated: March 7, 2016)

High-stress Si_3N_4 nanoresonators have become an attractive choice for electro- and optomechanical devices. Membrane resonators can achieve quality factor (Q) - frequency (f) products exceeding 10^{13} Hz, enabling (in principle) quantum coherent operation at room temperature. String-like beam resonators possess conventionally 10 times smaller $Q \cdot f$ products; however, on account of their much larger Q -to-mass ratio and reduced mode density, they remain a canonical choice for precision force, mass, and charge sensing, and have recently enabled Heisenberg-limited position measurements at cryogenic temperatures. Here we explore two techniques to enhance the Q -factor of a nanomechanical beam. The techniques relate to two main loss mechanisms: internal loss, which dominates for large aspect ratios and $f \lesssim 100$ MHz, and radiation loss, which dominates for small aspect ratios and $f \gtrsim 100$ MHz. First we show that by embedding a nanobeam in a 1D phononic crystal, it is possible to localize its flexural motion and shield it against radiation loss. Using this method, we realize $f > 100$ MHz modes with $Q \sim 10^4$, consistent with internal loss and contrasting sharply with unshielded beams of similar dimensions. We then study the $Q \cdot f$ products of high-order modes of mm-long nanobeams. Taking advantage of the mode-shape dependence of stress-induced ‘loss-dilution’, we realize a $f \approx 4$ MHz mode with $Q \cdot f \approx 9 \cdot 10^{12}$ Hz. Our results can extend room temperature quantum coherent operation to ultra-low-mass 1D nanomechanical oscillators.

Silicon nitride (SiN) nanomembranes and beams have emerged as striking exceptions to the empirical $Q \propto V^{1/3}$ scaling of solid-state mechanical oscillators [1]. Much of the recent history of this development can be traced to the ‘discovery’ that a commercial TEM slide made of 100 nm-thick LPCVD Si_3N_4 , forming a membrane resonator, can realize a room temperature $Q \cdot f > 6 \cdot 10^{12}$ Hz as well as ppm-level optical loss [2, 3]. The former constitutes a basic requirement for quantum-coherent evolution (since in this case the oscillator’s frequency f is larger than its thermal decoherence rate, $k_B T/hQ$), while the latter enables integration into a high finesse optical cavity, allowing for quantum-limited displacement readout and actuation [4, 5]. Encouraged by these prospects, considerable effort has been made to understand the source of high Q in SiN films. It is now generally accepted to be the large (~ 1 GPa) tensile stress resulting from LPCVD, which increases the elastic energy stored in the film without changing the material loss tangent [6–9] (a concept in fact dating back to mirror pendulum supports in gravitational wave interferometers [10]). Exploiting this insight, radio frequency membranes with room temperature $Q \cdot f > 10^{13}$ Hz have recently been realized, using a combination of high order modes [3, 11], stress engineering [12], and acoustically-shielded supports [13, 14].

In this report we study two strategies for reducing the dissipation of a high-stress SiN nanobeam, the 1D analog of a membrane which is in principle capable of $Q \cdot f > 10^{13}$ Hz with orders of magnitude lower mass and significantly reduced mode density, making it suitable for precision mass [16], charge [17], and force [18] sensing, in addition to quantum optomechanics experiments [2, 19]. The major challenge associated with nanobeams is their small form factor, which makes it difficult to transduce their motion. Towards this end, we employ

a microcavity-based near-field sensor [2] capable of non-invasive thermal noise measurements with $\text{fm}/\sqrt{\text{Hz}}$ resolution. Our first strategy is to pattern short ($< 10 \mu\text{m}$), very-high-frequency (> 100 MHz) nanobeams [20], for which an important source of loss is acoustic radiation. To address this challenge, we pattern the nanobeam as a defect in a 1D phononic crystal (PnC). When the frequency of a beam mode coincides with a band-gap of the PnC, the latter acts as an acoustic shield, effectively localizing flexural motion and suppressing radiation loss [21–23]. Using this strategy, we realize localized flexural modes with effective mass $m < 1$ pg, $f > 100$ MHz and $Q \sim 10^4$, consistent with internal loss and contrasting sharply with unshielded beams of similar dimensions.

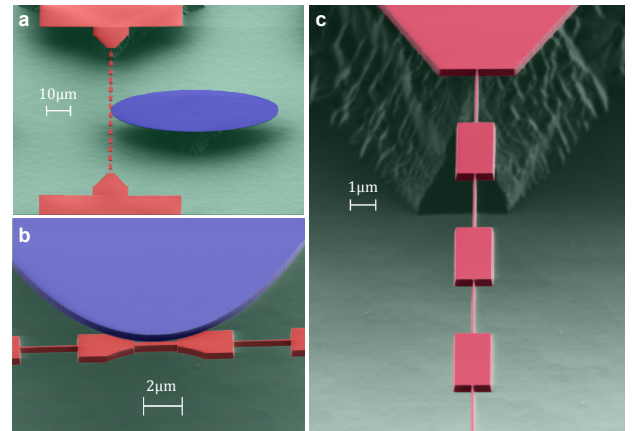


FIG. 1. **A nanobeam embedded in a 1D phononic crystal.** SEM images of the device. False-coloring is used to distinguish the Si substrate (green), the micro-patterned SiN nanobeam (red) and a SiN microdisk (blue). The microdisk is used to optically probe the beam’s displacement [2].

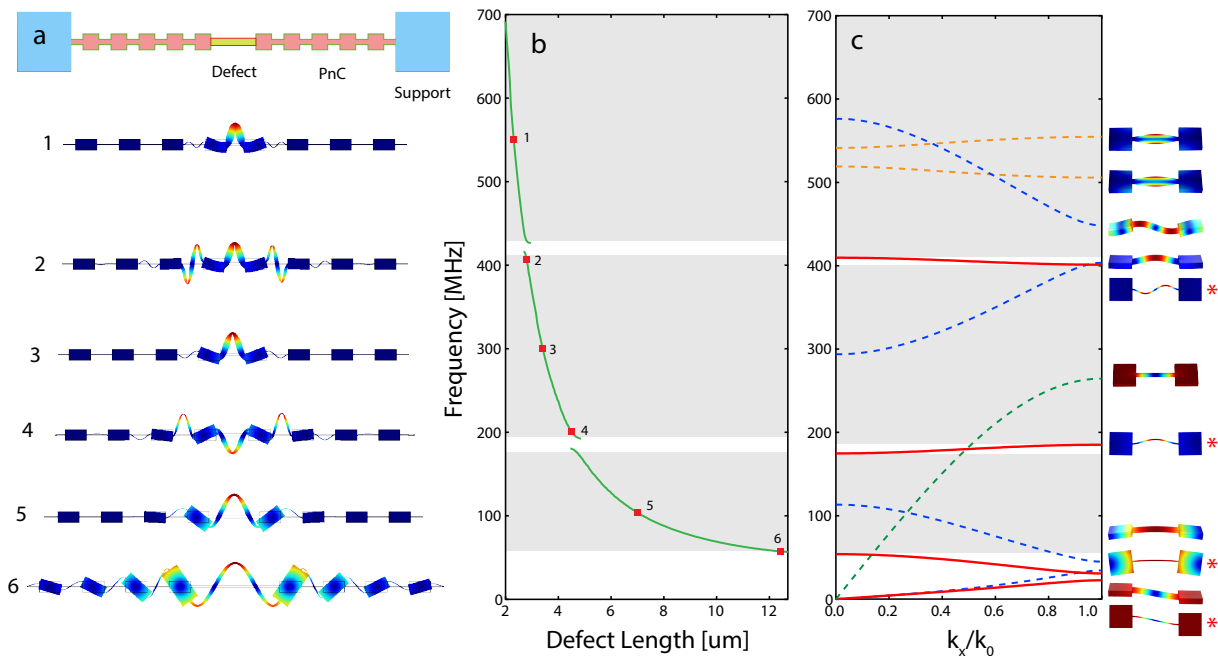


FIG. 2. **Simulation of defect modes and the phononic crystal bandgap.** (a) Schematic diagram of the device (top view), consisting of a nanobeam (green) patterned as a defect in a 1D phononic crystal (pink). Unit cell dimensions used in this work are $(h_1, L_1) = (100 \text{ nm}, 3 \mu\text{m})$ for the short segment and $(h_2, L_2) = (1.5 \mu\text{m}, 3 \mu\text{m})$ for the long segment. The SiN thickness of all devices is 400 nm. (b) Simulated fundamental eigenfrequency of a defect beam with in-plane thickness $h = 100 \text{ nm}$ and length $L = 2 - 16 \mu\text{m}$. Gray regions indicate bandgaps for in-plane flexural modes. Six representative modes are highlighted; their FEM-simulated modeshapes are plotted on the left. (c) Dispersion diagram of the phononic crystal. Curves represent different modes of the unit cell, color-coded according to symmetry (red, blue, green, and orange correspond to in-plane, out-of-plane, breathing, and torsional modes, respectively). Gray regions correspond to pseudo-bandgaps for in-plane modes.

Our second strategy is to study the high order modes of mm-long nanobeams, which exhibit enhanced $Q \cdot f$ due to tensile stress. We demonstrate that by appropriate choice of beam length and mode order, it is possible to realize $m \sim 10 \text{ pg}$, $f \sim 10 \text{ MHz}$ modes with a ‘quantum-enabled’ $Q \cdot f \approx 10^{13} \text{ Hz}$, a regime previously accessed only by $m \sim 10 \text{ ng}$ membrane resonators [3, 11, 13].

We first consider the device shown in Fig. 1. Here a high-stress Si_3N_4 thin film has been patterned into a 1D PnC with a beam-like defect at its center. From the standpoint of the beam, the crystal acts like a radiation shield [13, 14, 24], the performance of which is determined by the band structure of the box-shaped unit cell. A simulation of the dispersion diagram of the unit cell is shown in Fig. 2c, with lines of different color corresponding to modes of the cell with different symmetries. In this work, we consider only in-plane flexural modes because of their compatibility with displacement readout (using the microcavity-based sensor shown in blue in Fig. 1). Pseudo-bandgaps for in-plane symmetry are indicated by gray shading in Fig. 2c. The presence of a bandgap implies strong reflection of waves from the PnC. It also implies the support of localized defect modes. To illustrate this concept, a simulation of the fundamental flexural mode of a beam embedded in a 14-element PnC

is shown in Fig. 2b. Dimensions of the beam and unit cell are given in the caption. The beam’s length is varied to span the frequency range of the three bandgaps shown in Fig. 2c. Qualitatively, it is evident that modes which are well-centered in a bandgap (1,3,5) exhibit strong confinement. Conversely, modes near the edge of a bandgap (2,4,6) penetrate deeply into the PnC. This is because the defect modes start to hybridize with the in-plane modes of the unit cell, shown as red curves in Fig. 2c.

Our central claim is that localized defect modes will exhibit reduced radiation loss and similar effective mass relative to unshielded beams. To demonstrate this concept, shielded and unshielded beams of various lengths were fabricated (see [25]) and tested. To probe mechanical displacement, an elliptical microdisk cavity is patterned next to each beam, separated by $\sim 80 \text{ nm}$. Whispering gallery modes of the microdisk are excited with a detuned 1550 nm laser field using a tapered optical fiber, enabling evanescent displacement readout [2] with an imprecision of $\sim 1 \text{ fm}/\sqrt{\text{Hz}}$. All measurements were performed in a vacuum chamber at 10^{-4} mbar in order to reduce gas damping. In conjunction with the relatively large cavity linewidth of $\sim 1 \text{ GHz}$ (mitigating radiation pressure effects), this enables non-invasive thermal noise measurements for beams as short as $4 \mu\text{m}$.

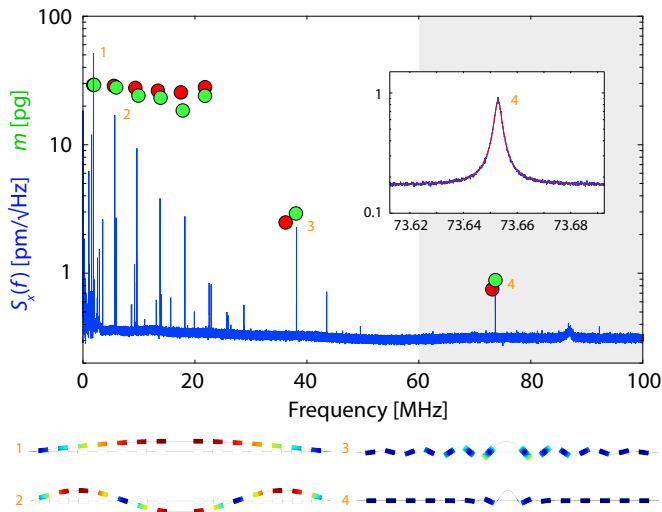


FIG. 3. **Broadband displacement spectrum of a PnC-shielded nanobeam.** A beam length of $8.25 \mu\text{m}$ is shown. FEM-simulations of four representative mode shapes are plotted below. Green points above selected peaks indicate the inferred effective mass. Red points are obtained from an FEM model. The absolute magnitude of the displacement spectrum and the effective mass is estimated by bootstrapping the latter to an FEM model (red points) of the effective mass for mode #1. Shaded regions correspond to the PnC bandgaps in Fig. 2. Inset: Magnified displacement spectrum of the localized (defect) mode, fitted to a Lorentzian.

As a demonstration of spatial mode confinement, the thermal displacement noise spectrum of a $5 \mu\text{m}$ -long defect embedded in a $100 \mu\text{m}$ -long, 14-cell PnC is presented in Fig. 3. The fundamental in-plane mode of the defect appears at 74 MHz, situated within a large, spectrally quiet window coinciding with the pseudo-bandgap of the PnC. The small effective mass of the defect mode manifests in the relatively large area beneath the thermal noise peak $\langle x^2 \rangle \approx k_B T / (4m\pi^2 f^2)$. Comparing $(\langle x^2 \rangle f^2)^{-1}$ for the defect mode to that of adjacent peaks (green points) reveals a 1000-fold decrease in m relative to the fundamental in-plane mode of the extended structure. Quantitative agreement of this scaling with an FEM simulation (red points, assuming a point-like probed at the midpoint of the defect) corroborates an estimated effective mass of $m \approx 1 \text{ pg}$ for the localized mode. The corresponding fitted mechanical linewidth is $\gamma = 5.1 \text{ kHz}$ ($Q \equiv f/\gamma = 1.4 \cdot 10^4$), giving access to a low thermal-noise-limited force sensitivity of $8\pi k_B T m \gamma = (0.7 \text{ fN}/\sqrt{\text{Hz}})^2$.

To assess the performance of the PnC as an acoustic shield, we have made a comprehensive study of Q vs f for shielded and unshielded beams of various lengths, using thermal noise measurements as in Fig. 3. Results are compiled in Fig. 4. Green and red points correspond to shielded and unshielded beams with lengths of $L = 12.2 - 4.1 \mu\text{m}$ and $10.5 - 90.5 \mu\text{m}$, respectively, comprising a total of 121 independent devices. The most striking feature is a sharp transition at $f_0 \sim 50 \text{ MHz}$, cor-

responding to $L \sim 10 \mu\text{m}$, at which the Q of unshielded beams changes from $Q \propto f^{-1}$ to a $Q \propto e^{-\alpha(f-f_0)}$. By contrast, shielded beams with $L < 10 \mu\text{m}$ exhibit a roughly constant Q , suggesting a qualitatively different loss mechanism compared to unshielded beams.

To understand the scaling of Q in Fig. 4, we consider a model of the form $Q^{-1} = Q_{\text{int}}^{-1} + Q_{\text{rad}}^{-1}$, where Q_{int} and Q_{rad} are models of loss due to internal friction and radiation of acoustic waves (phonon tunneling [5]) into the solid-state supports, respectively. We first consider internal loss, adopting a standard model that treats the film as an anelastic plate subject to cyclic loading [6–10]. In this approach, friction is treated as a delay between internal strain and stress (i.e., a complex Young’s modulus, E) [26]. The enhanced Q of stressed films is related to a renormalization of the total elastic energy, viz., adding tensile stress σ contributes an energy due to elongation, $U_{\text{elong}} \propto \sigma$, without substantially increasing the energy stored in bending, $U_{\text{bend}} \propto E$ (which gives rise to dissipation) [6]. The Q of a stressed film is thus enhanced relative to the unstressed case $Q_0 = \text{Re}[E]/\text{Im}[E]$ by approximately $Q/Q_0 \approx 1 + U_{\text{elong}}/U_{\text{bend}}$. The magnitude of the ‘loss-dilution’ factor Q/Q_0 depends on the stressed mode shape. For the string-like modes of stressed beams with thickness $h \ll L$, it can be shown that [6, 8, 9]

$$Q_{\text{int}}(\sigma, n) \approx Q_0 \left(1 + \left(\underbrace{2\lambda}_{\text{clamping}} + \underbrace{n^2 \pi^2 \lambda^2}_{\text{antinode}} \right)^{-1} \right) \quad (1)$$

where $\lambda = (h/L)\sqrt{E/12\sigma}$. Underbrackets here indicate

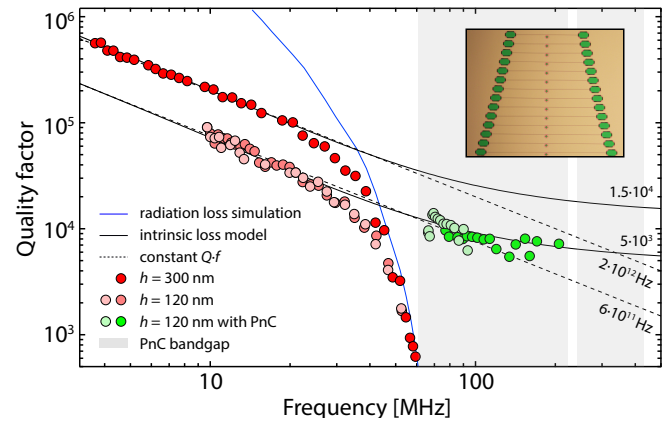


FIG. 4. **Quality factor of nanobeams with and without PnC shield.** Q versus f for the fundamental mode of nanobeams of various lengths ($L \approx 4 - 90 \mu\text{m}$). Green (red) points correspond to beams with (without) a PnC shield. Solid black lines are a single parameter fit to the internal loss model in Eq. (1), using Q_{int} as the fit parameter. Dashed black lines indicate constant $Q \cdot f$. The solid blue line is an FEM simulation of radiation loss for the unshielded beams. Shaded regions correspond to the PnC bandgaps in Fig. 2. The inset shows a sample chip containing a typical set of devices with different beam length, in this case without a PnC.

contributions due to bending at the clamping points and at the antinodes of the flexural mode, respectively, which depends on the mode order, n . The value of λ can be estimated from the dispersion relation

$$f(\sigma, n) \approx f_0 n \sqrt{(1 + n^2 \pi^2 \lambda^2)}, \quad (2)$$

where $f_0 \approx (1/2L)\sqrt{\sigma/\rho}$.

Eq. (1) and Eq. (2) are used to model the internal loss of beams with two widths ($h = 120, 300$ nm) in Fig. 4 (solid black lines). A value of $\lambda \approx 5 \cdot (h/L)$ is obtained by fitting measurements of f versus n to Eq. (2) (see Fig. 5). A value of $Q_0 \approx 5 \cdot 10^3 \cdot (h/100 \text{ nm})$ is obtained by bootstrapping to the $Q \propto f^{-1}$ scaling of long ($\lambda \ll 1$) unshielded beams. The inferred surface loss coefficient of $Q_0/h \approx 50 \text{ nm}^{-1}$ agrees well with the findings of Villanueva *et al.* [9]; however, Q_0 cannot be accessed directly with unshielded beams due to the large deviation from the internal loss model for $f \gtrsim 50$ MHz ($L \lesssim 10 \mu\text{m}$). Remarkably, the Q of shielded beams (green points) recovers to the expected internal loss scaling for $f \sim 50 - 200$ MHz ($L \sim 4 - 12 \mu\text{m}$), suggesting that the loss mechanism is acoustic radiation.

To confirm that the deviation from the internal loss model in Fig. 4 is due to acoustic radiation, we have conducted a no-free-parameter finite element simulation using COMSOL (for details see [25]). The geometry and stress-profile of the beam and PnC are determined from SEM imaging. The result of the simulation is shown as a solid blue line Fig. 4 and agrees qualitatively well with the data. Notably, the cutoff frequency for radiation losses depends sensitively on the geometry of the beam near the end-supports, as well as the support pillars (also included in the model). Chamfering the beam at its ends, as shown in Fig. 1 reduces the knee to $f \sim 50$ MHz, which is lower than has been observed for beams of similar dimensions with no end-chamfer [20].

Having addressed the challenge of reducing radiation loss in short, VHF beams, we now study a strategy for achieving high $Q \cdot f$ while keeping m fixed, by using higher order modes. Assuming $\lambda \ll 1$ and treating n as a continuous variable in Eq. (1) and Eq. (2), the maximum $Q \cdot f$ is obtained at $n_{\text{opt}} \approx \sqrt{2}/(\pi^2 \lambda)$ and is given by

$$\frac{Q_0 f_0}{\sqrt{8\pi^2 \lambda^3}} \approx 1.2 \cdot 10^{13} \text{ Hz} \cdot \frac{Q_0/h}{50 \text{ nm}^{-1}} \sqrt{\frac{L}{1 \text{ mm}} \frac{100 \text{ nm}}{h}} \cdot \left(\frac{\sigma}{0.8 \text{ GPa}}\right)^{\frac{5}{4}} \left(\frac{300 \text{ GPa}}{E}\right)^{\frac{3}{4}} \sqrt{\frac{2.7 \frac{\text{kg}}{\text{cm}^3}}{\rho}}. \quad (3)$$

Therefore high $Q \cdot f$ may be obtained by using high order modes of long and thin beams. We note that demonstrations of high-stress Si_3N_4 membranes with $Q \cdot f > 10^{13}$ Hz also exploit this scaling, with the mode index n in Eq. (1) and Eq. (2) replaced by $n^2 \rightarrow n^2 + m^2$. For diagonal modes ($n = m$), this results in an increase of Eq. (3) by a factor of $\sqrt{2}$. Interestingly, the conventionally higher $Q \cdot f$ reported for membranes as compared to

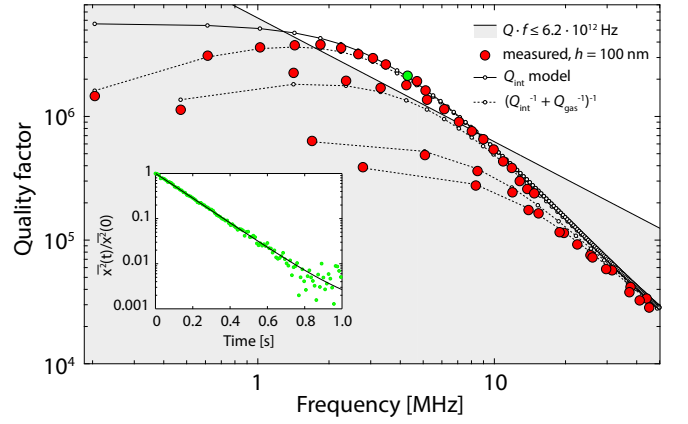


FIG. 5. **Quality factor versus mode order for long high-stress SiN nanobeams.** Q versus frequency for the odd-ordered flexural modes of nanobeams with lengths $L = 1.28, 0.55, 0.15,$ and 0.095 mm. Gray shading indicates $Q \cdot f < k_B \cdot 300 \text{ K}/h = 6.2 \cdot 10^{12}$ Hz. Black lines correspond to models for Q including internal loss (Eq. (1)) and an estimated gas damping rate of $\gamma_{\text{gas}} = 0.15 \text{ Hz}$ ($Q_{\text{gas}} = f/(0.15 \text{ Hz})$), using $\lambda = 5.5 \cdot h/L$. Inset: Ringdown measurement used to obtain the green point, $Q \cdot f \approx 9.0 \cdot 10^{12}$.

nanobeams appears to be related to the fact that larger membranes ($L \sim 1$ mm) have been studied [3, 8, 11].

To explore the prediction made in Eq. (3), we have measured $Q(n)$ and $f(n)$ for odd-ordered modes of unshielded beams with thickness $h = 100$ nm and lengths varying from $L = 0.95 - 1.28$ mm. Results are shown in 5. To mitigate systematic error associated with the sub-Hz mechanical linewidths, in this case Q was extracted from ringdown measurements. To perform a ringdown, the beam is resonantly excited using a piezo located beneath the sample chip; the drive is then shuttered off while displacement is continuously recorded using a network analyzer (with bandwidth $B \gg \gamma$). For the longest beam, $L = 1.28$ mm, we observe a maximum of $Q \cdot f \approx 9.0 \cdot 10^{12}$ for $n = 21$ ($f \approx 4$ MHz). We compare this to a model curve for $Q(n) \cdot f(n)$ (solid black line) based on a value of $\lambda = 5 \cdot h/L$ estimated by fitting the dispersion relation $f(n)$ (Eq. (2)). The model predicts $Q(n_{\text{opt}}) \cdot f(n_{\text{opt}})$ to within 10%, but qualitatively overestimates Q for lower frequencies. This discrepancy is due to gas damping, which contributes a systematic additional damping of $\gamma_{\text{gas}} \approx 0.15$ Hz.

We emphasize that while the concept of PnC acoustic shielding has recently been explored in the context of nanomembranes [13, 14] and nanobeams [24], our results, to the best of the authors' knowledge, represent the first explicit demonstration that the intrinsic Q of a nanomechanical resonator can be recovered in the presence of otherwise dominant radiation loss. Moreover, the value of $Q \cdot f \approx 9.0 \cdot 10^{12}$ demonstrated in Fig. 5 establishes a new benchmark for high-stress SiN nanobeams. In conjunction with the large zero-point motion and sparse mode density of nanobeams, and building on recent advances in

near-field cavity optomechanical coupling [4, 19], we envision application of these dissipation engineering strategies towards a new generation of quantum optomechanics experiments based on Heisenberg-limited measurements [19], perhaps even at room temperature. Nanoscale PnCs are furthermore readily extended to alternative materials such as diamond [28], opening the door for studying the microphysics of internal loss [29]. PnC-shielded nanoresonators may also find application as high frequency mechanical filters and oscillators [30, 31].

The authors thank Dr. Michael Zervas and Dr. Zdenek Benes for fabrication advice. All samples were fabricated at the CMi (Center of MicroNanotechnology) at EPFL. Research was carried out with support from an ERC Advanced Grant (QuREM), from the Swiss National Science Foundation and through grants from the NCCR of Quantum Engineering (QSIT). D.J.W. acknowledges support from the European Commission through a Marie Skłodowska-Curie Fellowship (IIF project 331985).

-
- [1] M. Imboden and P. Mohanty, *Phys. Rep.* **534**, 89 (2014).
- [2] B. M. Zwickl, W. E. Shanks, A. M. Jayich, C. Yang, A. C. Bleszynski Jayich, J. D. Thompson, and J. G. E. Harris, *Appl. Phys. Lett.* **92**, 103125 (2008).
- [3] D. Wilson, C. Regal, S. Papp, and H. Kimble, *Phys. Rev. Lett.* **103**, 207204 (2009).
- [4] J. D. Thompson, B. M. Zwickl, A. M. Jayich, F. Marquardt, S. M. Girvin, and J. G. E. Harris, *Nature* **452**, 72 (2008).
- [5] T. P. Purdy, R. W. Peterson, and C. A. Regal, *Science* **339**, 801 (2013).
- [6] Q. P. Unterreithmeier, T. Faust, and J. P. Kotthaus, *Phys. Rev. Lett.* **105**, 027205 (2010).
- [7] S. Schmid, K. D. Jensen, K. H. Nielsen, and A. Boisen, *Phys. Rev. B* **84**, 165307 (2011).
- [8] P.-L. Yu, T. Purdy, and C. Regal, *Phys. Rev. Lett.* **108**, 083603 (2012).
- [9] L. G. Villanueva and S. Schmid, *Phys. Rev. Lett.* **113**, 227201 (2014).
- [10] G. I. González and P. R. Saulson, *J. Acoust. Soc. Am.* **96**, 207 (1994).
- [11] S. Chakram, Y. S. Patil, L. Chang, and M. Vengalattore, *Phys. Rev. Lett.* **112**, 127201 (2014).
- [12] R. A. Norte, J. P. Moura, and S. Gröblacher, *arXiv preprint arXiv:1511.06235* (2015).
- [13] Y. Tsaturyan, A. Barg, A. Simonsen, L. G. Villanueva, S. Schmid, A. Schliesser, and E. S. Polzik, *Opt. Exp.* **22**, 6810 (2014).
- [14] P.-L. Yu, K. Cicak, N. Kampel, Y. Tsaturyan, T. Purdy, R. Simmonds, and C. Regal, *App. Phys. Lett.* **104**, 023510 (2014).
- [2] G. Anetsberger, O. Arcizet, Q. P. Unterreithmeier, R. Rivière, A. Schliesser, E. M. Weig, J. P. Kotthaus, and T. J. Kippenberg, *Nat. Phys.* **5**, 909 (2009).
- [16] K. Jensen, K. Kim, and A. Zettl, *Nat. Nano.* **3**, 533 (2008).
- [17] A. N. Cleland and M. L. Roukes, *Nature* **392**, 160 (1998).
- [18] H. Mamin and D. Rugar, *App. Phys. Lett.* **79**, 3358 (2001).
- [19] D. Wilson, V. Sudhir, N. Piro, R. Schilling, A. Ghadimi, and T. Kippenberg, *Nature* **524**, 325 (2015).
- [20] X. Huang, X. Feng, C. Zorman, M. Mehregany, and M. Roukes, *New J. Phys.* **7** (2005).
- [21] D. Goettler, M. Su, Z. Leseman, Y. Soliman, R. Olsson, and I. El-Kady, *J. App. Phys.* **108**, 084505 (2010).
- [22] S. Mohammadi, A. A. Eftekhar, R. Pourabolghasem, and A. Adibi, *Sens. Act. A: Phys.* **167**, 524 (2011).
- [23] F.-C. Hsu, J.-C. Hsu, T.-C. Huang, C.-H. Wang, and P. Chang, *App. Phys. Lett.* **98**, 143505 (2011).
- [24] J. Chan, A. H. Safavi-Naeini, J. T. Hill, S. Meenehan, and O. Painter, *App. Phys. Lett.* **101**, 081115 (2012).
- [25] Supplementary Information.
- [26] C. Zener, *Phys. Rev.* **53**, 90 (1938).
- [4] R. Schilling, H. Schütz, A. Ghadimi, V. Sudhir, D. J. Wilson, and T. J. Kippenberg, *arXiv preprint arXiv:1601.06745* (2016).
- [28] B. Khanaliloo, H. Jayakumar, A. C. Hryciw, D. P. Lake, H. Kaviani, and P. E. Barclay, *arXiv:1502.01788* (2015).
- [29] S. Groeblacher, A. Trubarov, N. Prigge, G. D. Cole, M. Aspelmeyer, and J. Eisert, *Nat. Comm.* **6**, 7606 (2015).
- [30] J. Teva, A. G. Berini, A. Uranga, J. Verd, F. Torres, J. Lopez, J. Esteve, F. Pérez-Murano, and N. Barniol, *Proc. IEEE MEMS 2008* (2008).
- [31] X. Feng, C. White, A. Hajimiri, and M. L. Roukes, *Nat. Nano.* **3**, 342 (2008).

Supplementary information for “Dissipation engineering of high-stress silicon nitride nanobeams”

I. SAMPLE FABRICATION

A. Overview

Nanobeam-microdisk samples as shown in Fig. 1 of the main text are fabricated according to the procedure outlined in Fig. 1. The process begins with a series of low pressure chemical vapor deposition (LPCVD) steps on a 4" CZ Si wafer. 400 nm of stoichiometric Si_3N_4 (SiN) is deposited at 800°C , followed by 100 nm of amorphous Si (a-Si) at 500°C (to be used as a hard mask). The microdisk and nanobeam are patterned on top of the a-Si film by electron beam lithography, in 100 nm of HSQ. The pattern is transferred into the a-Si film (creating a hard mask for the subsequent SiN etch) using a HBr etch process. The pattern is then transferred into the SiN film by reactive ion etching, using an SPTS APS Dielectric Etcher and CHF_3 chemistry. The process is concluded by undercutting the microdisk and nanobeam with KOH, followed by critical point drying.

B. Fabrication considerations related optomechanical coupling

The fabrication process was developed and optimized with two goals in mind: (1) to minimize the in-plane gap (x) between the nanobeam and the microdisk and (2) to minimize the sidewall roughness of the microdisk. Small x is desirable as it gives rise to a large parametric (optomechanical) coupling $G = \partial\omega_c/\partial x$ between the lateral position of the beam and the frequency ω_c of the microdisk whispering gallery mode (WGM) [1]. For beams with in-plane thickness much smaller than the operating wavelength λ , it can be shown that $G \propto e^{-x/x_{ev}}$, where $x_{ev} \sim \lambda/10$ is the in-plane evanescent decay length of the WGM [2]. Thus a design gap of $x < 100$ nm was chosen in conjunction with an operating wavelength of $\lambda \approx 1550$ nm. Low sidewall roughness is desirable in order to reduce the possibility of

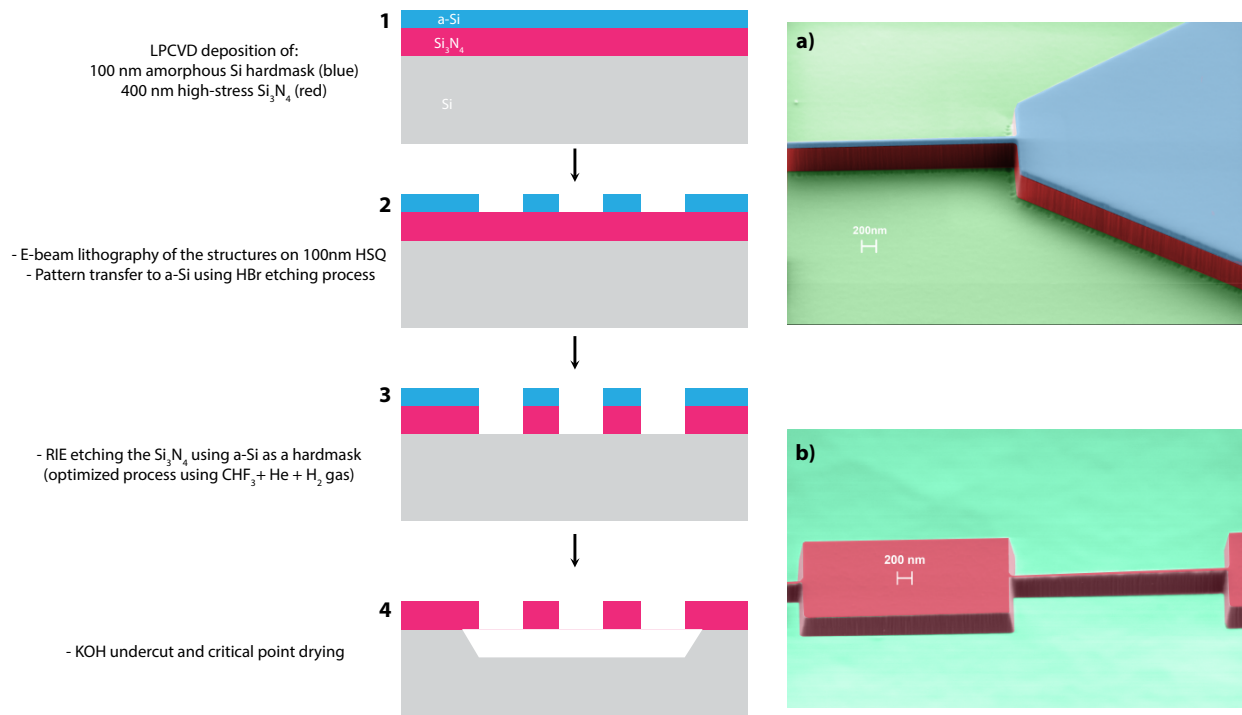


FIG. 1. **Fabrication process flow.** (1-4) Illustration of the main fabrication steps. (a) False-colored SEM images of the device after step 3, with green, blue, and red indicating Si, a-Si, and Si_3N_4 , respectively. (b) False-colored SEM image of a single PnC unit cell after KOH undercut (step 4).

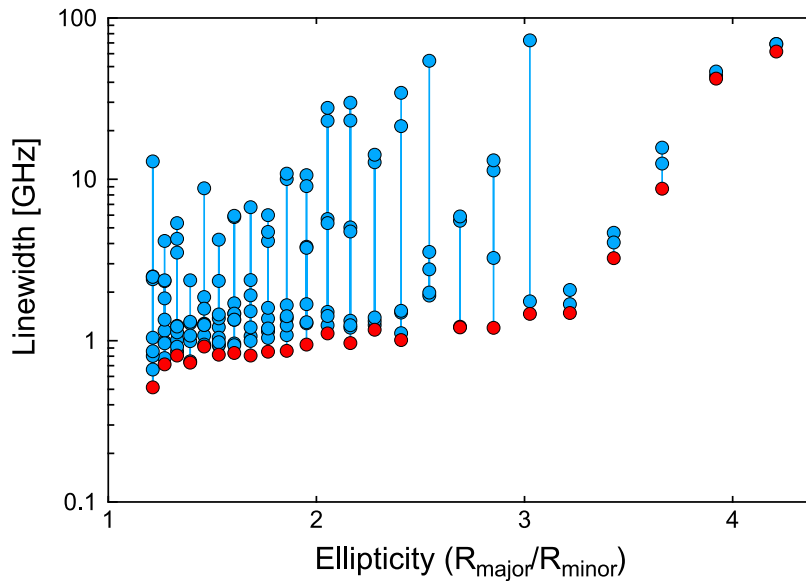


FIG. 2. **Optical loss of elliptical microdisk cavities.** Measured WGM linewidth for microdisks with a fixed circumference of $31 \mu\text{m}$ and ellipticity (ratio of the major and minor radii) varying from 1 to 4. WGMs of different polarization and radial order were measured, giving rise observed variation in optical loss for each ellipticity. Red points highlight the best value from each measurement set.

WGM loss (κ) due to Rayleigh scattering from the disk's surface [3]. Collectively, increasing G and reducing κ was crucial to achieving the high sensitivity displacement measurements shown in Fig. 3 and employed in Figs. 4-5 of the main text. For example, in Fig. 3 of the main text, the thermomechanical signal-to-noise (in this case dominated by electronic detector noise) is proportional to $(G^2 P / \kappa)^2$, where P is the optical input power [1].

The requirements for etching optically smooth sidewalls separated by $x < 100 \text{ nm}$ depends on the thickness of the SiN film. We chose a $t = 400 \text{ nm}$ -thick film as a compromise between achieving a large WGM evanescence and low WGM radiation loss. Achieving a vertical $x < 100 \text{ nm}$ gap thus required etching SiN with an aspect ratio much better than 1:4. We found that achieving this aspect ratio while maintaining an optically smooth surface was difficult with standard RIE etching techniques (employing standard e-beam resists), due to mask erosion. It is for this reason that a-Si was employed as a secondary hard mask. a-Si provides high selectivity ($>1:10$) relative to SiN in RIE as well as high resistance to mask erosion. Thus we have achieved gaps as small as $x \approx 80 \text{ nm}$ and relatively smooth sidewalls, characterized by optical quality factors in excess of 10^5 in the absence of a beam (see Fig. 2). For the results shown in Figs. 3-5 of the main text, we employed elliptical microdisks with a fixed circumference of approximately $30 \mu\text{m}$, an ellipticity (major radius over minor radius) ranging from 1 to 4, and $x = 80 - 200 \text{ nm}$. Typical intrinsic optical linewidths of $\kappa/2\pi = 1 - 10 \text{ GHz}$ were observed. An estimate of $G(x = 100 \text{ nm}) \sim 100 \text{ MHz/nm}$ is obtained by approximating the microdisk WGM profile with the analytical form of a microtoroid WGM, as discussed in [2, 4].

II. ACOUSTIC RADIATION LOSS MODEL

A. Overview

The radiation loss model shown in Fig. 4 of the main text was obtained by computing the complex eigenfrequency spectrum of the mechanical structure surrounded by numerically implemented PML (perfectly matched layer, corresponding to a perfectly impedance matched and absorbing boundary). We used the COMSOL Structural Mechanics Finite Element Analysis software package for this simulation. The modeled structure is shown in gray in Fig. 2a, and includes the SiN defect beam, SiN PnC, SiN support pads, the Si pillars beneath each support pad, a half-spherical section of the Si substrate. The blue shell in Fig. 2a corresponds to the PML. By placing the PML far from the nanobeam, we ensure that reflection of acoustic waves from the supports is accounted for in the simulation. We also ensure that the size of the PML is large enough that its own reflection coefficient is negligible [5, 6]. Visualization of acoustic radiation into the PML is shown in Fig. 2c. Radiation loss manifests as an imaginary component of each

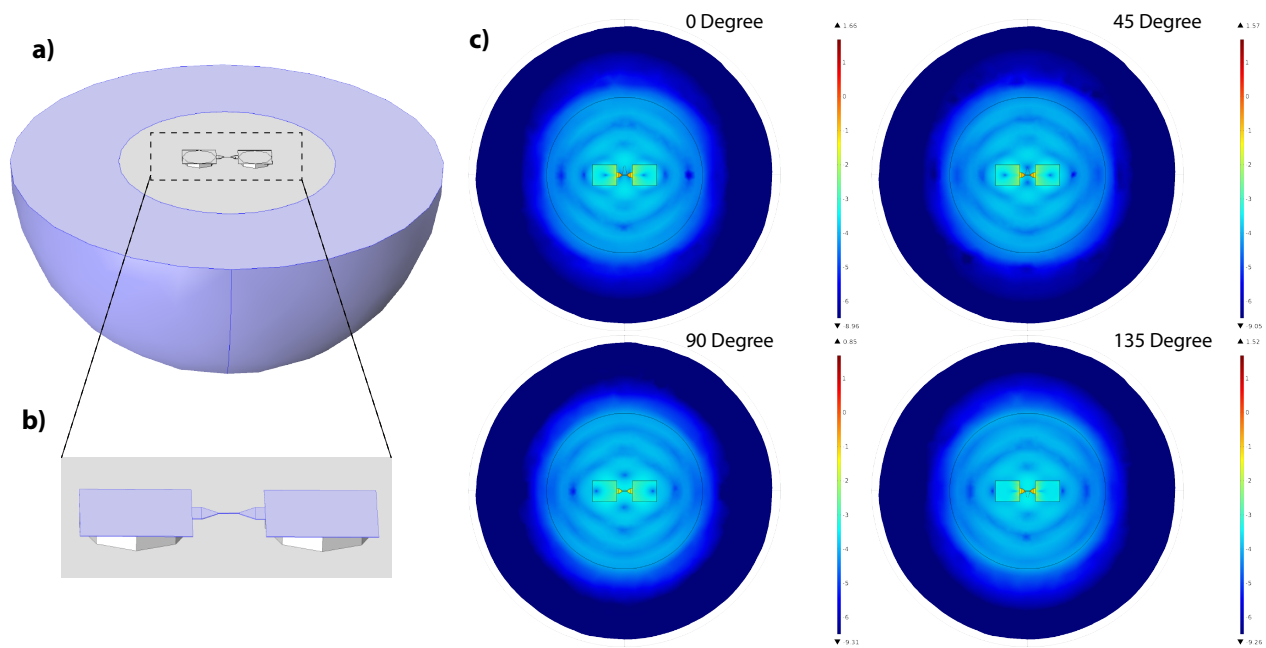


FIG. 3. **FEM simulation of acoustic radiation loss.** (a) Geometry of the simulated device. The gray volume indicates the mechanical structure and the blue volume is a PML. (b) Magnified image of the mechanical structure, including the SiN beam and PnC shield, SiN support pads, Si pillars beneath the support pads, and a portion of the underlying Si substrate. A stress relaxation simulation is performed in order to determine the stress profile of this structure before solving for eigenmodes. (c) Visualization of acoustic waves propagating into the Si substrate and being absorbed by PML. The amplitude of the mechanical strain field is illustrated by logarithmic color-coding.

numerically computed eigenfrequency, Ω_m . The eigenfrequency of the defect mode is identified based on its mode shape. Radiation-loss-limited Q -factors (blue curve in Fig. 4 of the main text) are obtained from the formula:

$$Q_{\text{rad}} = \frac{\text{Re}[\Omega_m]}{2 \cdot \text{Im}[\Omega_m]}. \quad (1)$$

The location of the knee point in the model of Q_{rad} versus f in Fig. 4 of the main text depends on the dimensions of the extended mechanical structure, in particular that of Si pillars and the trapezoidal end-points of the beam (c.f. Fig. 1a in the main text). The blue curve shown in Fig. 4 of the main text employs dimensions obtained from SEM imaging and uses no fit parameters.

B. Role of number of unit cells

The acoustic impedance of the PnC depends on the number of unit cells used. We employed a 7-cell PnC to obtain the results described in the main text. This choice was based on a model of Q_{rad} versus number of cells. An example is shown in Fig. 4: here a $2.3 \mu\text{m}$ defect with a frequency of 542 MHz is embedded in the 3rd bandgap of the PnC described in Fig. 2 of the main text. As illustrated in the figure, only 3 cells are required to reduce the radiation loss by a factor of 10^6 , to a value ~ 6 orders of magnitude larger than Q_{int} ; also shielding evidently saturates at ~ 6 cells. A conservative choice of 7 cells was made in the experiment to allow for design imperfections.

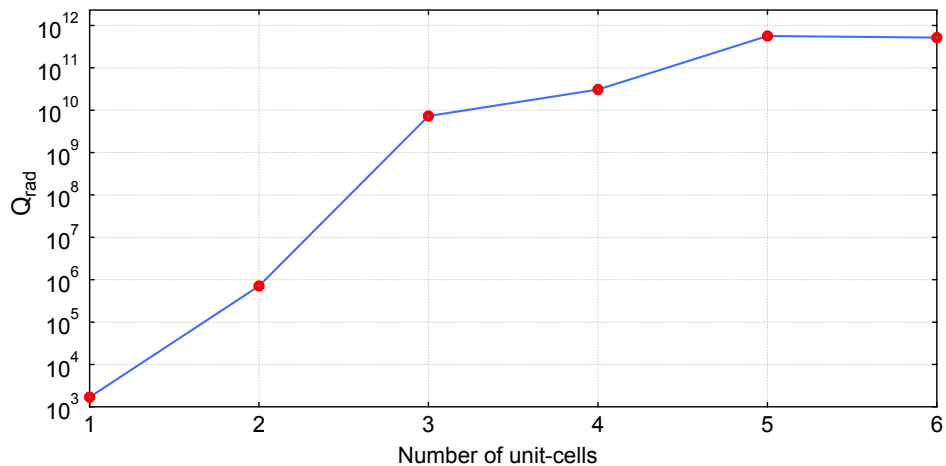


FIG. 4. **Numerical simulation of acoustic radiation loss versus number of unit cells.** Results shown are for a 2.3 μm -long defect beam with a frequency of 542 MHz. The cell dimensions and band diagram are the same as in Fig. 2 of the main text.

-
- [1] M. Aspelmeyer, T. J. Kippenberg, and F. Marquardt, *Rev. Mod. Phys.* **86**, 1391 (2014).
 [2] G. Anetsberger, O. Arcizet, Q. P. Unterreithmeier, R. Rivière, A. Schliesser, E. M. Weig, J. P. Kotthaus, and T. J. Kippenberg, *Nat. Phys.* **5**, 909 (2009).
 [3] M. Borselli, K. Srinivasan, P. E. Barclay, and O. Painter, *App. Phys. Lett.* **85**, 3693 (2004).
 [4] R. Schilling, H. Schütz, A. Ghadimi, V. Sudhir, D. J. Wilson, and T. J. Kippenberg, *arXiv preprint arXiv:1601.06745* (2016).
 [5] I. Wilson-Rae, *Phys. Rev. B* **77**, 245418 (2008).
 [6] I. Wilson-Rae, R. Barton, S. Verbridge, D. Southworth, B. Ilic, H. Craighead, and J. Parpia, *Phys. Rev. Lett.* **106**, 047205 (2011).